Numerical Simulation of Supersonic and Turbulent Combustion with Transverse Sonic Fuel Injection

Mohammed Kamel[1], Farouk Owis[2], Moumen Idres[3], Aly Hashem[4]

Aerospace Engineering Department - Faculty of Engineering
Cairo University, Giza, Egypt
[1]mkamel@eng.cu.edu.eg
[2]fowis@eng.cu.edu.eg (Corresponding Author)
[3]midres@iium.edu.my
[4]aafhashem@eng.cu.edu.eg

Abstract Complicated interacting flow features such as shock-wave, boundary-layer and shock induced combustion are simulated numerically in the current study to investigate the effect of the transverse sonic fuel injection on the air-fuel mixing and flame stabilisation. The flow is modelled using the Reynolds-averaged Navier-stocks (RANS) equations, where chemical kinetics model is employed to compute the finite rates of chemical reactions. Turbulence is modelled using the Baldwin-Lomax algebraic model. Finite-volume scheme is applied where the convective fluxes are discretised by second order accurate Roe?s scheme using MUSCL approach. Second order accurate Runge-Kutta method is used for the time-integration. Turbulent and chemically-reacting supersonic flow of hydrogen-air mixture over a ramp is simulated and the results show good agreement with the experimental data and the published numerical simulations In addition, air-hydrogen flow is studied in a single strut scramjet engine, where mixing and flame holding processes are carried out using fuel transverse sonic injection.

Keywords: Scramjet Engines; Computational Fluid Dynamics; Chemically-Reacting Flows; Reynolds-Averaged Navier-Stocks; Turbulent Flows; Supersonic Combustion

Biographical Notes:
– Mohammed Kamel is a Lecturer Assistant in Cairo University, where he received his MSc in 2009. Currently, he is a PhD student in the University of Notre Dame, USA. His areas of interests are computational fluid dynamics, reacting flows simulation, and turbulence modelling.
– Farouk Owis is an Associate Professor in Cairo University, where he received his MSc in 1993. In 1999, he received his PhD from Old Dominion University, USA. His fields of interest cover computational fluid dynamics, turbomachinery, jet engine propulsion, and renewable energy.
– Moumen Idres received his BSc and MSc in Cairo University in 1992 and 1995, respectively. In 1999, he received his PhD from Old Dominion University, USA. He is on leave from Cairo University. Currently, he is an Assistant Professor in the International Islamic University Malaysia. He has research publications in aerospace propulsion, vehicle power systems, combustion and computational fluid mechanics.
– Aly Hashem has been a Professor of Aircraft Propulsion, Cairo University since 2005. He received his MSc and PhD from Cranfield Institute of Technology, School of Mechanical Engineering, UK in 1974 and 1977, respectively. His areas of interests concern turbo-machinery, jet engine propulsion, renewable energy and combustion.

1 Introduction

Flows with chemical reactions are of interest across a wide range of engineering applications including supersonic combustion, space vehicle reentry, and rocket plume problems. A great amount of effort has been focused in the areas of algorithm development and thermo-chemical modeling for these flows. The modeling of chemically reacting turbulent flows at supersonic speeds has been attempted by many investigators (2; 3). However, the physical and mathematical complexities of this problem have prevented the development of satisfactory models for the turbulence and combustion mechanisms and their influence on each other in a compressible flowfield. A relatively recent review by Cinnella and Grossman (4) provides details on numerical methods for chemically reacting flows. There is still a continuing effort to better understand these complex flow phenomenon.

The objective of the current study is to develop an accurate numerical tool for the simulation of turbulent and supersonic chemically-reacting flows. The code is used to investigate numerically the effect of transverse fuel injection on the air-fuel mixing and flame holding. This work is motivated by the need to simulate flowfields present in a typical supersonic combustion ramjet (SCRAMJET) engine where flame-holding in the supersonic flowfield is attained by providing the necessary activation energy for combustion initiation in very small fraction of time. Shock-induced combustion, or plasma torches are the most feasible flame-holding candidates. However, transverse sonic fuel injection into supersonic air inlet flow is one of the most efficient techniques suggested to enhance both air-fuel mixing and flame holding, as introduced by Drummond (1). Transverse sonic injection of the gaseous fuel into the air supersonic stream leads to rapid air-fuel mixing. Transverse injection configuration can be manipulated to obtain optimum heat release for a wide range of flight Mach numbers.

The developed code is utilized to simulate the chemically reacting turbulent flows inside scramjet engine. The code is validated by considering several test cases. The code is then used to resolve the complicated flowfield accompanying the sonic transverse injection of Helium into supersonic air flow. The results are compared with the previous results of Kraemer and Rogers experiment reported by Durmmond et al. (26). In addition, the turbulent chemically non-reacting flows inside scramjet engines are also simulated in the current study. This non-reacting case is simulated for turbulent flow inside single strut scramjet engine as introduced by Drummond and Weidner (26).

Different features of turbulent flows, which are generally modeled using unsteady Navier-Stokes equations, can be resolved by time-averaging approaches such as Reynolds averaged Navier-Stocks equations (RANS). It can also be resolved using space-averaging approaches such as Large Eddy Simulation (LES). Large Eddy Simulation solves the filtered spatial-averaged large-scale components of turbulence (on the order of 90% of transport components), where the small scales are modeled. On the other hand, Direct Numerical Simulation (DNS) considers all flow features with all relevant length scales to be resolved from the smallest eddies to scales on the order of the physical dimensions of the problem domain. Despite the shortcomings associated with the statistical representation of time-averaging RANS closures, RANS equations still show efficiency in most test cases. As, it requires much less computational effort than that required by LES or DNS approaches (5; 6). The mathematical model used in the current simulation is the unsteady Reynolds-Averaged Navier-Stocks equations (RANS). Finite-volume discretization is employed for the numerical integration of the governing equations. The second-order Roe's scheme is used for spatial discretization. Total variation diminishing are achieved by using minmode limiter. A two-step second order accurate Runge-Kutta is used for the time integration. Point-implicit scheme is applied for the chemical source term to reduce the stiffness of the system.

Turbulence modeling based on Boussinseq's assumption, are divided into numerous categories according to the number of the additional partial differential equations. There are the field two-equations turbulence models such as (k-ϵ) model (7; 8), and (k-ω) model (9). In addition, there are the One-Equation Turbulence Models such as Baldwin-Barth model (10). Zero-Equation models require an algebraic equation solution to obtain the turbulent flow properties such as Cebeci-Smith model (11) and Baldwin-Lomax model (12). Algebraic models are widely used due to its simplicity and robustness although they give inaccurate estimations in strong flow separations (13). In the current study, zero- equation of Baldwin-Lomax are used to calculate the turbulent eddy viscosity.

In supersonic combustion, the order of magnitude of characteristic time of the chemical reactions is much less than that of flow residence time. Therefore, stiffness of the source terms arises from the great gap between the time scales of the coupled governing equations. Full implicit treatment of the governing equations for two-dimensional flows leads to the solution of simultaneous equations in pent-block diagonal matrix form. Different factorization methods are testified in fully implicit solver (14). It is found that the iterative method of Lower-Upper Symmetric Gauss-Siedel (LUSGS) method (15) shows the fastest convergence rates for implicit solvers of 2D domains. In order to reduce the computational efforts of inverting the flow Jacobians, the convective and viscous flow fluxes are treated explicitly, where only the chemical source term is solved implicitly. This method is well-known as Chemistry-Implicit or Point-Implicit. It is introduced by Curtiss and Hirschfelder (16). In this case, a mono-block diagonal matrix will be solved. Thus, the computational effort is greatly reduced.

Flux-vector and flux-difference splitting schemes are numerically applied by Grossman et al (17) to simulate chemically and thermally non-equilibrium one-dimensional flows. More extensions for multi-dimensional problems are presented by Walters et al. (18), where two reacting mechanisms of H_2-air are studied. Bussing and Murman (20; 21) used a finite volume point-implicit method with multi-grid accelerator. Shuen and Yoon (22) employed fully implicit finite-volume with lower-upper symmetric successive over-relaxation scheme (LUSSOR). Their model is coupled with chemical kinetics model of 8-species and 14-reactions model (23). Eklund et al. (24) studied relative merits of Adam and Runge-Kutta schemes. Partial implicit method and the global two-step chemistry model (19) was used successfully by Drummond, et al. (25) to calculate premixed Hydrogen-air reacting flow using a spectral method. Drummond and Weidner solved transverse sonic injection of hydrogen into supersonic air flow in a single strut scramjet engine using the finite difference scheme of MacCormak with complete chemical reaction model (26). Chitsomboon and Tiwari (27; 28) used also a finite difference method for similar problems.

2 Mathematical Modeling

2.1 Governing Equations

The governing Equations are the Reynolds time averaging Navier Stocks equations. The conservative non-dimensional form of RANS equations for two-dimensional flow is written as follows,

$$\frac{\partial Q}{\partial t}+\frac{\partial E}{\partial x}+\frac{\partial F}{\partial y}+\alpha H = \\ =\frac{\partial E_v}{\partial x}+\frac{\partial F_v}{\partial y}+\alpha H_v+S \quad (1)$$

Where α is a logical switch between planar and 2D axisymmetric two-dimensional flows. S represents the chemical source term.

$$Q=[\rho,\rho u,\rho v,\rho E_t,\rho Y_m]^T \quad (2)$$

$$E=\begin{bmatrix}\rho u\\ \rho u^2+P\\ \rho uv\\ \rho H_t u\\ \rho Y_m u\end{bmatrix} \qquad F=\begin{bmatrix}\rho v\\ \rho uv\\ \rho v^2+P\\ \rho H_t v\\ \rho Y_m v\end{bmatrix} \quad (3)$$

$$E_v=\begin{bmatrix}0\\ \tau_{xx_p}\\ \tau_{xy}\\ \tau_{xx_p}u+\tau_{xy}v-q_x\\ -d_{mx}\end{bmatrix}$$

$$F_v=\begin{bmatrix}0\\ \tau_{xy}\\ \tau_{yy_p}\\ \tau_{xy}u+\tau_{yy_p}v-q_y\\ -d_{my}\end{bmatrix} \quad (4)$$

$$\alpha=\begin{cases}0, & \text{Planar 2D Flow}\\ 1, & \text{Axisymmertic 2D Flow}\end{cases} \quad (5)$$

$$H=\frac{1}{y}\begin{bmatrix}\rho v\\ \rho uv\\ \rho v^2\\ \rho H_t v\\ \rho Y_m v\end{bmatrix} \quad (6)$$

$$H_v=\begin{bmatrix}0\\ \frac{\tau_{xy}}{y}+\frac{\partial \tau_a}{\partial x}\\ \frac{\tau_{yy_p}+\tau_a-\tau_{\theta\theta}}{y}+\frac{\partial \tau_a}{\partial y}\\ \frac{\tau_{xy}u+\left[\tau_{yy_p}+\tau_a\right]v-q_y}{y}+\left(\frac{\partial(\tau_a u)}{\partial x}+\frac{\partial(\tau_a v)}{\partial y}\right)\\ \frac{-d_{my}}{y}\end{bmatrix} \quad (7)$$

$$S=[0,0,0,0,\dot{\omega}_m]^T \quad (8)$$

The governing equations are non-dimensionalized with respect to reference values of the characteristic dimensions of the problem which are denoted L_{ref} , ρ_{ref} , V_{ref} , T_{ref}.

2.2 Thermodynamic Model

The mixture enthalpy and internal energy are calculated by summation of the species contributions.

$$h = \sum_{m=1}^{n_s} Y_m h_m \qquad e = \sum_{m=1}^{n_s} Y_m e_m \tag{9}$$

The non-dimensional enthalpy for individual species is determined by:

$$h_m = \frac{1}{V_{ref}^2}\left[h_{f_m}^o + \int_{T_o}^{T^*} c_{p_m} \mathrm{d}T^*\right] \tag{10}$$

where: $T^* = T.T_{ref}$, and $h_{f_m}^o$ is the species heat of formation. We assume that specific heat coefficient for each species (c_{p_m}) is a polynomial function in temperature (T) as given by Mcbride et al. (31). The total mixture enthalpy and internal energy are described as:

$$H_t = \frac{h_{f_{mix}}^o + \int_{T_o}^{T^*} c_{p_{mix}} d\tau + \frac{(u^2+v^2)}{2}}{V_{ref}^2} \tag{11}$$

$$E_t = \frac{h_{f_{mix}}^o + \int_{T_o}^{T^*} (c_{p_{mix}} - R_{mix})\, d\tau + \frac{(u^2+v^2)}{2}}{V_{ref}^2} \tag{12}$$

where $h_{f_{mix}}^o, c_{p_{mix}}, \mathrm{and R_{mix}}$ are the mixture's heat of formation, heat coefficient at constant temperature, and gas constant:

$$\begin{aligned} h_{f_{mix}}^o &= \sum_{m=1}^{ns} Y_m h_{f_m}^o \\ c_{p_{mix}} &= \sum_{m=1}^{ns} Y_m c_{p_m} \\ R_{mix} &= \sum_{m=1}^{ns} Y_m R_m \end{aligned} \tag{13}$$

The equation of state of the gaseous mixture can be written as,

$$P = \frac{T_{ref}}{V_{ref}^2}\rho R_{mix} T \tag{14}$$

where (h_s) and (e_s) are the mixture sensible enthalpy and sensible internal energy respectively will be defined as follows,

$$\begin{aligned} h_s &= h - h_{f_{mix}}^o = \int_{T_o}^{T^*} c_{p_{mix}} \mathrm{d}T^* \\ e_s &= e - h_{f_{mix}}^o = \int_{T_o}^{T^*} (c_{p_{mix}} - R_{mix})\, \mathrm{d}T^* \end{aligned} \tag{15}$$

It can be shown that:

$$h_s - e_s = \frac{P}{\rho} - \frac{R_{mix}}{V_{ref}^2} T_o \tag{16}$$

The reference temperature degree (T_o) is set to be the absolute zero to ensure positive sensible enthalpy and sensible internal energy and to enhance the stability of the numerical solution as recommended by Anderson (34). Also, the ratio of the mixture sensible enthalpy to the mixture internal energy is considered as the "*equivalent*" specific ratio of the multi-species mixture to simplify the complexity of the thermodynamic relations as discussed by Shuen and Yoon (22).

$$\gamma = \frac{h_s}{e_s} = \frac{\int_{T_o}^{T^*} c_{p_{mix}} \mathrm{d}T^*}{\int_{T_o}^{T^*} (c_{p_{mix}} - R_{mix})\, \mathrm{d}T^*} \tag{17}$$

So, the relation between the mixture pressure and density to the mixture sensible internal energy becomes,

$$\frac{P}{\rho} = e_s\,(\gamma - 1) \tag{18}$$

2.3 Turbulent Dynamic Viscosity Modeling

Algebraic Baldwin-Lomax turbulence model is applied to calculate the turbulent eddy coefficient eddy (μ_T). A two-layer turbulence model; where the turbulent dynamic viscosity coefficient (μ_T) is calculated with one of two different sets of algebraic equations depending on the distance (n) from boundary walls, or jets centerlines:

$$\mu_T = \begin{cases} \mu_{T_{in}}, & n \le n_{cross} \\ \mu_{T_{out}}, & n > n_{cross} \end{cases} \tag{19}$$

The turbulent viscosity profile μ_T for the two-layer model is calculated as follow,

$$\mu_T = \min\left(\mu_{T_{in}}, \mu_{T_{out}}\right). \tag{20}$$

- **Inner Region** In the inner region, eddy viscosity coefficient ($\mu_{T_{in}}$) is calculated in terms of the mixing length (l_{mix}), and the vorticity vector magnitude (ω) as follows,

$$\mu_{T_{in}} = \rho l_{mix}^2 \omega \tag{21}$$

where:

$$\omega = \sqrt{\left[\frac{\partial u}{\partial y} + \frac{\partial v}{\partial x}\right]^2} \tag{22}$$

$$l_{mix} = \kappa\ n\left(1 - e^{-n^+/A^+}\right) \tag{23}$$

The damping factor (e^{-n^+/A^+}) is eliminated for the cases of wakes and jets.

- **Outer Region** The eddy viscosity of the outer layer $(\mu_{T_{out}})$ is calculated as follows,

$$\mu_{T_{out}} = \rho K C_{cp} F_{wake} F_{Klep} \tag{24}$$

The normal distance (n) and velocity (V) are normalized to (n^+) and (u^+) using the friction velocity (u_τ) and flow variables at the wall surface.

$$u_\tau = \sqrt{\frac{\tau_w}{\rho_w}}, \quad n^+ = \frac{u_\tau \rho_w n}{\mu_{L_w}}, \quad u^+ = \frac{V}{u_\tau} \tag{25}$$

The other terms in equation (24) are written in the following form:

$$F_{wake} = min\left(n_{max}F_{max}, C_{wk}n_{max}\frac{u_{\text{diff}}^2}{F_{max}}\right) \tag{26}$$

$$F_{Kleb} = \left[1 + 5.5\left(\frac{nC_{Kleb}}{n_{max}}\right)^6\right]^{-1} \tag{27}$$

where (u_{diff}) is the difference between the maximum and minimum velocity magnitudes in the boundary layer. So in the wall-bounded domains the minimum velocity equals zero and $u_{\text{diff}} = V_{max}$. Besides, (F_{max}) is the max value of the intermediate function $F(n)$ along a certain line normal to the wall or normal to the centerline of the jet. This function is written as follows,

$$F(n) = \frac{1}{\kappa} l_{mix}\omega \tag{28}$$

$$F_{max} = \max_n\left[F(n)\right] \tag{29}$$

$$n_{max} = n|_{_{F_{max}}} \tag{30}$$

n_{max} is the normal distance (n) at which the function (F) reaches its maximum value. This turbulence approach consists of six closure constant listed below according to Baldwin and Lomax (12):

$$\begin{array}{ll} A^+ = 26 & C_{cp} = 1.6\ C_{Kleb} = 0.3 \\ C_{wk} = 0.25\ \kappa = 0.4 & K = 0.0168 \end{array} \tag{31}$$

In spite of the excellent performance of the Baldwin and Lomax method in solving attached flows, it predicts incorrectly the separation point location for strong pressure gradients. Degani and Schiff (13) added some modifications to the previous model to eliminate the reasons leading to the model deficiency when used in separated flows. They found that there are dramatic differences in the behavior of the intermediate function $F(n)$ in the attached and separated flows, which have considerable effects on the calculations. It is found that there is *one local maximum point* in the function $F(n)$, where the global maximum of the function (F_{max}) can be estimated. However, in separated flows, there will be *multiple local maxima*. By implementing equation (29)to get (F_{max}), the global maximum will be selected, which is not considered the right choice. The local maxima far away from the wall or jets represents recirculating zone of high vorticity magnitude. The right choice is to select the nearest local maximum from the wall or jet centerline to be used in the turbulence model calculations with the physical correct values of F_{max} and n_{max}.

2.4 Mass and Heat Fluxes Modeling

The diffusive mass fluxes d_{mx} and d_{my} of the m^{th} species in the x and y directions are written as follows,

$$\begin{aligned} d_{mx} &= \frac{-1}{Re_{ref}Sc_{ref}}\left(\rho\mathcal{D}_L + \frac{\mu_T}{Sc_T}Sc_{ref}\right)\frac{\partial Y_m}{\partial x} \\ d_{my} &= \frac{-1}{Re_{ref}Sc_{ref}}\left(\rho\mathcal{D}_L + \frac{\mu_T}{Sc_T}Sc_{ref}\right)\frac{\partial Y_m}{\partial y} \end{aligned} \tag{32}$$

$\mathcal{D}_L$ is the laminar mass diffusivity coefficient of m^{th} species into the mixture which is assumed constant for all species.. In addition, Sc_{ref} is the problem characteristic "Schmidt number", which is given as:

$$Sc_{ref} = \frac{\mu_{ref}}{\rho_{ref}\mathcal{D}_{ref}} \tag{33}$$

On the other hand, the heat fluxes in the x and y directions are written as follows,

$$\begin{aligned} q_x = \frac{1}{Re_{ref}}\Bigg[&\frac{-1}{(\gamma_{ref}-1)\,\mathbf{M}_{ref}^2 Pr_{ref}}k_L\frac{\partial T}{\partial x} \\ &- \frac{1}{Sc_{ref}}\sum_{m=1}^{n_s} h_m\rho\mathcal{D}_L\frac{\partial Y_m}{\partial x} - \frac{\mu_T}{Pr_T}\frac{\partial h}{\partial x}\Bigg] \\ q_y = \frac{1}{Re_{ref}}\Bigg[&\frac{-1}{(\gamma_{ref}-1)\,\mathbf{M}_{ref}^2 Pr_{ref}}k_L\frac{\partial T}{\partial y} \\ &- \frac{1}{Sc_{ref}}\sum_{m=1}^{n_s} h_m\rho\mathcal{D}_L\frac{\partial Y_m}{\partial y} - \frac{\mu_T}{Pr_T}\frac{\partial h}{\partial y}\Bigg] \end{aligned} \tag{34}$$

M_{ref} and Pr_{ref} are the reference values of "Mach number" and "Prandtl number" respectively. The turbulent terms of "Schmidt number" (Sc_T) and "Prandtl number" (Pr_T) are utilized to model the

mass and heat turbulent fluxes respectively. Both are set to be 0.9. Modeling of mass and heat laminar transport coefficients (i.e. $\mathcal{D}_L$ and k_L) is based on assuming constant values of the laminar terms of "Prandtl number"(Pr_L) and "Lewis number" (Le). Pr_L is assumed to be 0.72 according to ref. (28), while Le is set to unity. Based on the previous assumptions, k_L and $\mathcal{D}_L$ are determined as follows,

$$k_L = \frac{c_{p_{mix}}\ \mu_L}{Pr_L} \tag{35}$$

$$\mathcal{D}_L = \frac{k_L}{\rho\ Le\ c_{p_{mix}}} \tag{36}$$

2.5 Chemistry Modeling

Decoupling between chemistry and turbulence models is adopted in this study. The random fluctuations in the magnitudes of temperature and mass fractions are not considered in the calculations of the species source terms. For chemically reacting non-equilibrium air-Hydrogen system, the combustion process is modeled using a mechanism composed of a number of elementary reactions, not only one global reaction. Each elementary equation can be written as following:

$$\nu'_{m,r} X_m \underset{k_b}{\overset{k_f}{\rightleftharpoons}} \nu''_{m,r} X_m \tag{37}$$

(ν') and (ν'') are the stoichiometric coefficients of the reactants and products respectively of each elementary reaction of index (r), where $r = 1, 2, .., n_r$, where (n_r) is the total number of elementary reactions in the mechanism. (k_f) and (k_b) are the chemical reaction rates in the forward and backward directions respectively. The source term of each species of index ("m'') is calculated using the "law of mass action". It is written in the dimensionless form as follows,

$$\dot{\omega}_m = \frac{L_{ref}}{\rho_{ref} V_{ref}} \mathcal{M}_m \sum_{r=1}^{n_r} \left[\begin{array}{l} (\nu'_{m,r} - \nu''_{m,r}) * \\ * \left(k_{fr} \prod_{m=1}^{n_s} \left(\frac{\rho Y_m}{\mathcal{M}_m} \right)^{\nu'_{m,r}} + \right. \\ \left. \quad -k_{br} \prod_{m=1}^{n_s} \left(\frac{\rho Y_m}{\mathcal{M}_m} \right)^{\nu''_{m,r}} \right) \end{array} \right] \tag{38}$$

The forward reaction rate (k_f) is calculated using the Arrhenius' formula whose coefficients and the temperature exponent is determined experimentally. It is written for each elementary reaction of index (r) as follow,

$$k_{fr} = \mathcal{A}_r T^{\mathcal{N}_r} \exp\left(\frac{-E_{actv,r}}{\mathcal{R}\ T} \right) \tag{39}$$

Air-Hydrogen combustion system is modeled by using the two reactions mechanism suggested by Rogers and Chinitz (19). This two reactions model includes four reacting species (O_2, H_2O, H_2, and OH), besides Nitrogen N_2, which is assumed to be inert, because the mixture temperature is not too high to initiate the Nitrogen-Oxides formation;

$$O_2 + H_2 \underset{k_{b1}}{\overset{k_{f1}}{\rightleftharpoons}} 2\,OH \tag{40}$$

$$2\,OH + H_2 \underset{k_{b2}}{\overset{k_{f2}}{\rightleftharpoons}} 2\,H_2O \tag{41}$$

The forward reaction rates for the two reactions are written as follows,

$$\begin{aligned} k_{f1} &= \mathcal{A}_1 T^{-10} \exp\left(\frac{-4063.6485}{\mathcal{R}T^*} \right) \\ k_{f2} &= \mathcal{A}_2 T^{-13} \exp\left(\frac{-35499.4988}{\mathcal{R}T^*} \right) \end{aligned} \tag{42}$$

In equation (42), the units of the universal gas constant $(\mathcal{R})$ is $[kcal/kmole\ K]$. The pre-exponential coefficients for the elementary reaction are function of the equivalence ratio (ϕ), as follows,

$$\begin{aligned} \mathcal{A}_1 &= \left[8.917\phi + \tfrac{31.433}{\phi} - 28.95 \right] (10)^{44} \left[\tfrac{m^3/kmol}{\sec} \right] \\ \mathcal{A}_2 &= \left[2 + \tfrac{1.333}{\phi} - 0.833\phi \right] (10)^{58} \left[\tfrac{m^3/kmol}{\sec} \right] \end{aligned} \tag{43}$$

3 Numerical Treatment

The governing equations can be written in the computational domain in the following form:

$$\frac{\partial \overline{Q}}{\partial t} + \frac{\partial \overline{E}}{\partial \xi} + \frac{\partial \overline{F}}{\partial \eta} + \alpha \overline{H} = \frac{\partial \overline{E_v}}{\partial \xi} + \frac{\partial \overline{F_v}}{\partial \eta} + \alpha \overline{H_v} + \overline{S}, \tag{44}$$

where:

$$\begin{aligned} \overline{Q} &= \frac{1}{J} Q, \\ \overline{E} &= \frac{1}{J} (\xi_x E + \xi_y F), \quad \overline{F} = \frac{1}{J} (\eta_x E + \eta_y F), \\ \overline{E_v} &= \frac{1}{J} (\xi_x E_v + \xi_y F_v), \quad \overline{F_v} = \frac{1}{J} (\eta_x E_v + \eta_y F_v), \\ \overline{H} &= \frac{1}{J} H, \quad \overline{H_v} = \frac{1}{J} H_v, \quad \overline{S} = \frac{1}{J} S, \end{aligned} \tag{45}$$

The finite volume method is used to discretize the governing equations at each cell in the computational domain. Starting from equation (44), the integral vector form for cell of volume $(\mathbb{V})$ is described in the following form:

$$\begin{aligned} \iiint_{\mathbb{V}} \left[\frac{\partial \overline{Q}}{\partial t} + \frac{\partial \left(\overline{E} - \overline{E_v} \right)}{\partial \xi} + \frac{\partial \left(\overline{F} - \overline{F_v} \right)}{\partial \eta} \right] \mathrm{d}\mathbb{V} = \\ = \iiint_{\mathbb{V}} \overline{S} \mathrm{d}\mathbb{V} - \alpha \iiint_{\mathbb{V}} \left(\overline{H} - \overline{H_v} \right) \mathrm{d}\mathbb{V} \end{aligned} \tag{46}$$

In the current study, the finite-volume scheme is nodal-centered. The discrete integral vector form of the governing equation for an individual cell is formulated as follows,

$$\begin{aligned}\frac{\overline{Q}_{i,j}{}^{n+1} - \overline{Q}_{i,j}{}^{n}}{\Delta t} = \\ = -\frac{\overline{E}_{i+\frac{1}{2},j} - \overline{E}_{i-\frac{1}{2},j}}{\Delta\xi} - \frac{\overline{F}_{i,j+\frac{1}{2}} - \overline{F}_{i,j-\frac{1}{2}}}{\Delta\eta} \\ + \frac{\overline{E_v}_{i+\frac{1}{2},j} - \overline{E_v}_{i-\frac{1}{2},j}}{\Delta\xi} + \frac{\overline{F_v}_{i,j+\frac{1}{2}} - \overline{F_v}_{i,j-\frac{1}{2}}}{\Delta\eta} \\ -\alpha\overline{H}_{i,j} + \alpha\overline{H_v}_{i,j} + \overline{S}_{i,j}\end{aligned} \tag{47}$$

Roe's scheme presents an approximate solution for Riemann's problem (i.e. shock tube problem) at each cell face in order to resolve the flow variable discontinuities. Ideal gases frozen flows can be solved by Roe's scheme (32). This approach was extended by Grossman et. al (17) for chemically and thermally nonequilibrium one-dimensional flows, and then more extensions were presented by Walters et al. (18) for multi-dimensional flows.

In equation (47), $\overline{E}_{i\pm\frac{1}{2},j}$ and $\overline{F}_{i,j\pm\frac{1}{2}}$ are the convective fluxes at the cell faces in ξ-direction and η-direction, respectively. The general formulation of the convective flux at the cell interface involves the averaged value of the fluxes at the right and left sides of the face, in addition to the flux jump across the cell interface.

$$\overline{E}_{\mathbf{F}} = \frac{1}{2}\left(E^{\mathbf{R}} + E^{\mathbf{L}}\right) - \frac{1}{2}[\![E]\!] \tag{48}$$

The second term of wave speeds superposition ($[\![E]\!]$) in equation (48) can be decomposed into three terms as follows,

$$[\![E]\!] = [\![E]\!]_A + [\![E]\!]_B + [\![E]\!]_C \tag{49}$$

The averaging of the variable (f) between the left and right sides of the cell interface is defined by $\langle\ \rangle$. The value of the flow variable at the cell face, which is given by the subscript $\{\}_{\mathbf{F}}$, is the arithmetic average of the flow variables in the two adjacent mesh nodes;

$$\langle f\rangle = \frac{1}{2}\left(f^{\mathbf{R}} + f^{\mathbf{L}}\right) \tag{50}$$

$$f_{\mathbf{F}} = \frac{1}{2}\left(f_{\text{front node}} + f_{\text{back node}}\right) \tag{51}$$

On the other hand, the jump in the value of (f), across the cell interface, from the left to the right sides, will be defined as follows,

$$[\![f]\!] = \left(f^{\mathbf{R}} - f^{\mathbf{L}}\right) \tag{52}$$

In equation (49), $([\![E]\!]_A)$ represents the summation of the wave speeds in ξ-direction, corresponding to the (n_s+1) eigenvalues in ξ-direction. $([\![E]\!]_B)$ and $([\![E]\!]_C)$ correspond to the two last eigenvalues $(\mathcal{U} + c\,|\nabla\xi|)$ and $(\mathcal{U} - c\,|\nabla\xi|)$ respectively, where (c) is the speed of sound. The three vectors are expressed as follows,

$$\begin{aligned}[\![E]\!]_A = \\ = \frac{|\nabla\xi|_{\mathbf{F}}}{J_{\mathbf{F}}}\left|\widehat{\mathcal{U}'}\right| \left\{ \begin{bmatrix} \left([\![\rho]\!] - \frac{[\![P]\!]}{\widehat{c}^{\,2}}\right) \\ \left([\![\rho]\!] - \frac{[\![P]\!]}{\widehat{c}^{\,2}}\right)\widehat{u} \\ \left([\![\rho]\!] - \frac{[\![P]\!]}{\widehat{c}^{\,2}}\right)\widehat{v} \\ \left([\![\rho]\!] - \frac{[\![P]\!]}{\widehat{c}^{\,2}}\right)\widehat{H}_t - \frac{\widehat{c}^{\,2}}{(\widehat{\gamma}_{mix}-1)} \\ \left([\![\rho]\!] - \frac{[\![P]\!]}{\widehat{c}^{\,2}}\right)\widehat{Y}_m \end{bmatrix} + \right. \\ \left. + \widehat{\rho}\begin{bmatrix} 0 \\ [\![u]\!] + [\![\mathcal{U}']\!]\,\xi'_{x_{\mathbf{F}}} \\ [\![v]\!] + [\![\mathcal{U}']\!]\,\xi'_{y_{\mathbf{F}}} \\ \Theta_\xi \\ [\![Y_m]\!] \end{bmatrix} \right.\end{aligned} \tag{53}$$

$$\begin{aligned}[\![E]\!]_{B,C} = \frac{|\nabla\xi|_{\mathbf{F}}}{J_{\mathbf{F}}}\left|\left(\widehat{\mathcal{U}'} \pm \widehat{c}\right)\right| \cdot \\ \cdot \left(\frac{1}{\widehat{c}^{\,2}}\right)\left([\![P]\!] \pm \widehat{\rho}\,\widehat{c}\,[\![\mathcal{U}']\!]\right) \begin{bmatrix} 1 \\ \widehat{u} \pm \widehat{c}\,\xi'_{x_{\mathbf{F}}} \\ \widehat{v} \pm \widehat{c}\,\xi'_{y_{\mathbf{F}}} \\ \widehat{H}_t \pm \widehat{\mathcal{U}'}\,\widehat{c} \\ \widehat{Y}_m \end{bmatrix}\end{aligned} \tag{54}$$

where:

$$\widehat{\mathcal{U}'} = \frac{1}{|\nabla\xi|_{\mathbf{F}}}\left(\xi_{x_{\mathbf{F}}}\,\widehat{u} + \xi_{y_{\mathbf{F}}}\,\widehat{v}\right) \tag{55}$$

$$[\![\mathcal{U}']\!] = \mathcal{U}'^{\mathbf{R}} - \mathcal{U}'^{\mathbf{L}} \tag{56}$$

$$\mathcal{U}'^{\mathbf{R}} = \frac{\mathcal{U}^{\mathbf{R}}}{|\nabla\xi|_{\mathbf{F}}} \qquad \mathcal{U}'^{\mathbf{L}} = \frac{\mathcal{U}^{\mathbf{L}}}{|\nabla\xi|_{\mathbf{F}}} \tag{57}$$

$$\xi'_{x_{\mathbf{F}}} = \frac{\xi_{x_{\mathbf{F}}}}{|\nabla\xi|_{\mathbf{F}}} \qquad \xi'_{y_{\mathbf{F}}} = \frac{\xi_{y_{\mathbf{F}}}}{|\nabla\xi|_{\mathbf{F}}} \tag{58}$$

Also, (Θ_ξ) is the expression for:

$$\Theta_\xi = \widehat{u}\,[\![u]\!] + \widehat{v}\,[\![v]\!] - \widehat{\mathcal{U}'}\,[\![\mathcal{U}']\!] - \sum_{m=1}^{n_s}[\![Y_m]\!]\,\widehat{\psi}_m \tag{59}$$

The expression of the summation of the wave speeds in η-direction is represented in three terms. The first is $([\![F]\!]_A)$, which corresponds to the eigenvalue $(\mathcal{V})$ in η-direction. It is repeated for (n_s+1) times. The

other two are $(\llbracket F \rrbracket_B, \llbracket F \rrbracket_C)$, corresponding to the remaining eigenvalues $(\mathcal{V} \pm c\,|\nabla\eta|)$:

$$\llbracket F \rrbracket_A = \\ = \frac{|\nabla\eta|_{\mathbf{F}}}{J_{\mathbf{F}}} \left|\widehat{\mathcal{V}}'\right| \left\{ \begin{array}{l} \left(\llbracket\rho\rrbracket - \frac{\llbracket P \rrbracket}{\widehat{c}^{\,2}}\right) \begin{bmatrix} 1 \\ \widehat{u} \\ \widehat{v} \\ \widehat{H}_t - \frac{\widehat{c}^{\,2}}{(\widehat{\gamma}_{mix}-1)} \\ \widehat{Y}_m \end{bmatrix} + \\ +\widehat{\rho} \begin{bmatrix} 0 \\ \llbracket u \rrbracket + \llbracket \mathcal{V}' \rrbracket \eta'_{x_{\mathbf{F}}} \\ \llbracket v \rrbracket + \llbracket \mathcal{V}' \rrbracket \eta'_{y_{\mathbf{F}}} \\ \Theta_\eta \\ \llbracket Y_m \rrbracket \end{bmatrix} \end{array} \right. \quad (60)$$

$$\llbracket F \rrbracket_{B,C} = \frac{|\nabla\eta|_{\mathbf{F}}}{J_{\mathbf{F}}} \left|\left(\widehat{\mathcal{V}}' \pm \widehat{c}\right)\right| \cdot \\ \cdot \left(\frac{1}{\widehat{c}^{\,2}}\right) \left(\llbracket P \rrbracket \pm \widehat{\rho}\,\widehat{c}\,\llbracket \mathcal{V}' \rrbracket\right) \begin{bmatrix} 1 \\ \widehat{u} \pm \widehat{c}\,\eta'_{x_{\mathbf{F}}} \\ \widehat{v} \pm \widehat{c}\,\eta'_{y_{\mathbf{F}}} \\ \widehat{H}_t \pm \widehat{\mathcal{V}}'\,\widehat{c} \\ \widehat{Y}_m \end{bmatrix} \quad (61)$$

Determination of the spatial accuracy of the flux-difference splitting scheme is determined by the calculation of the right and left sides of the cell interface in terms of the nearest mesh nodes surrounding the cell face midpoint. The general form of the primitive-variable calculation at the cell face$(i+\frac{1}{2}, j)$ as an example, for first order accurate upwind scheme and second order upwind TVD scheme, is written as follows,

$$\begin{aligned} f^{\mathbf{R}}_{i+\frac{1}{2},j} &= f_{i+1,j} - \tfrac{\varepsilon}{2}\psi(r^{\mathbf{R}}_{i+\frac{1}{2},j})\,[f_{i+2,j} - f_{i+1,j}] \\ f^{\mathbf{L}}_{i+\frac{1}{2},j} &= f_{i,j} \quad + \tfrac{\varepsilon}{2}\psi(r^{\mathbf{L}}_{i+\frac{1}{2},j})\,[f_{i,j} - f_{i-1,j}] \end{aligned} \quad (62)$$

where:

$$\varepsilon = \begin{cases} 0, & 1^{st} \text{ order accuracy} \\ 1, & 2^{nd} \text{ order accuracy (MUSCL Approach).} \end{cases} \quad (63)$$

Equation (62) defines the value of the primitive variable for right and left side of the cell faces. To satisfy Total Variation Diminishing (TVD), slope nonlinear limiters $\psi(r)$ are utilized here to eliminate the numerical oscillations formed around the flow discontinuities because of the second order space accurate schemes, and to save the monotonicity of the solution to match with the physical one. The flow variable slope $(r)$for the left and right sides of the faces of the control volume is calculated as follows,

$$r^{\mathbf{R}}_{i+\frac{1}{2},j} = \frac{f_{i+1,j} - f_{i,j}}{f_{i+2,j} - f_{i+1,j}}, r^{\mathbf{L}}_{i+\frac{1}{2},j} = \frac{f_{i+1,j} - f_{i,j}}{f_{i,j} - f_{i-1,j}}, \quad (64)$$

Minmode limiter is the employed slope limiter. It is defined by a logical expression in terms of the slope of the flow variable, i.e. $\psi \equiv \psi(r)$, so it belongs to the discontinuous slope limiters of flux limiters which are *not* expressed by a smooth continuous function. The minmode limiter is written as,

$$\psi(r) = max\,[0, min\,(1, r)]\,. \quad (65)$$

The source of stiffness resulted from the chemical characteristic time is eliminated and the computational effort is reduced using point-implicit scheme. This scheme suggested by Curtiss and Hirschfelder (16) by treating the chemical source term implicitly and flow fluxes explicitly. The discretized governing equation can be written as follows,

$$\begin{aligned} &\frac{\overline{Q}_{i,j}{}^{n+1} - \overline{Q}_{i,j}{}^{n}}{\Delta t} = \\ &= -\frac{\overline{E}^n_{i+\frac{1}{2},j} - \overline{E}^n_{i-\frac{1}{2},j}}{\Delta\xi} - \frac{\overline{F}^n_{i,j+\frac{1}{2}} - \overline{F}^n_{i,j-\frac{1}{2}}}{\Delta\eta} \\ &+\frac{\overline{E_v}^{n+1}_{i+\frac{1}{2},j} - \overline{E_v}^{n}_{i-\frac{1}{2},j}}{\Delta\xi} + \frac{\overline{F_v}_{i,j+\frac{1}{2}}{}^{n+1} - \overline{F_v}^{n}_{i,j-\frac{1}{2}}}{\Delta\eta} \\ &-\alpha\overline{H}^n_{i,j} + \alpha\overline{H_v}^n_{i,j} + \overline{S}^{n+1}_{i,j} \end{aligned} \quad (66)$$

Time linearization of second order accuracy is implemented to the chemical source term as follows,

$$\begin{aligned} \overline{S}_{i,j}{}^{n+1} &= \overline{S}_{i,j}{}^{n} + \left(\frac{\partial\overline{S}}{\partial\overline{Q}}\right)_{i,j} \left(\frac{\partial\overline{Q}}{\partial t}\right)_{i,j} \Delta t + \mathcal{O}\Delta t^2 \\ &= \overline{S}_{i,j}{}^{n} + \overline{\mathbf{H}}_{i,j} \left(\overline{Q}_{i,j}{}^{n+1} - \overline{Q}_{i,j}{}^{n+1}\right) + \mathcal{O}\Delta t^2 \end{aligned} \quad (67)$$

where $(\overline{\mathbf{H}}_{i,j})$ is the chemical source Jacobian in the computational domain. By treating the source term implicitly, the time step is no longer restricted by the characteristic time of the chemical reactions. Also, applying point-implicit scheme leads to solving mono-block diagonal matrix. The chemical sources are also considered only dependent upon the species concentrations only.

Although the chemical source term is solved implicitly, the value of the CFL number (σ) does not exceed one, due to the explicit treatment of the other flow terms. According to Drummond et al. (25) and Chitsomboon et al. (29), CFL (Courant-Friedrichs-Lewy) condition can be written in the following form:

$$\Delta t_{_{local}} = \sigma \left\{ \left(\frac{|\mathcal{U}| + c\,|\nabla\xi|}{\Delta\xi}\right) + \left(\frac{|\mathcal{V}| + c\,|\nabla\eta|}{\Delta\eta}\right) \right\}^{-1}. \quad (68)$$

4 Results

4.1 Turbulent Chemically Reacting Flows in a Ramped Duct

The numerical code is also used to solve turbulent premixed Hydrogen-air supersonic flow in a two-dimensional ramped duct shown in figure (1). The duct walls are assumed to be adiabatic. The incoming flow is premixed hydrogen-air at stoichiometric ratio. The problem is solved for two different inlet temperatures; below and above the ignition threshold which is equal to 1000 $[K]$. The inlet conditions are described as follows,

$$\begin{aligned} T_{in} &= \begin{cases} 900\ [K] & \text{Test Case 1} \\ 1200\ [K] & \text{Test Case 2} \end{cases} \\ P_{in} &= 101325\ [Pa], \\ \mathbf{M}_{in} &= 4.0, \quad \phi_{in} = 1.0, \end{aligned} \tag{69}$$

The reference length is set to be the longitudinal length of the duct, while the other reference variables to equal to the inlet flow properties as shown below:

$$\begin{aligned} L_{ref} &= 3\ [cm], \\ \rho_{ref} = \rho_{in}, \quad T_{ref} &= T_{in}, \quad V_{ref} = V_{in}, \\ \mu_{ref} = \mu_{L_{in}}, \quad k_{ref} &= k_{L_{in}}, \quad \mathcal{D}_{ref} = \mathcal{D}_{L_{in}}, \end{aligned} \tag{70}$$

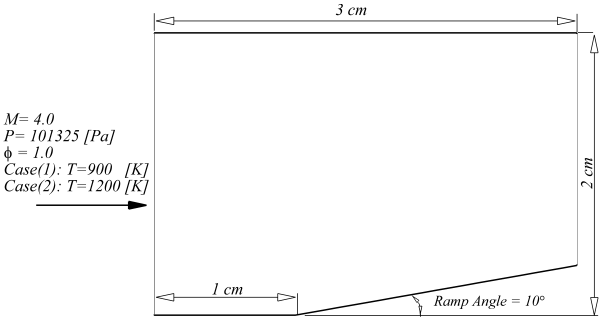

Figure 1 Schematic diagram of hydrogen-air flow in 2D ramped duct

For each of the two cases, three different sets of calculations using different meshes, whose sizes are 31×51, 61×51 and 91×51. They have different mesh spacing in the stream-wise direction. The most refined mesh is shown in figure (2).

4.1.1 Non-reacting Inlet Flow Test Case

In the first test case the inlet temperature is below the ignition threshold of hydrogen-air combustion system (1000 $[K]$). But, it rises after the oblique shock wave and in the viscous layers near wall surface, to become high enough, i.e. (greater than 1000 $[K]$), for combustion initiation. The formed oblique shock is considered as *detonation wave*, as it is responsible in the reaction excitation and sustainability.

Local time-stepping is used for the pseudo time-integration, where CFL number equals to ($\sigma = 0.1$). It is clear from figure (3) that convergence is attained after a relatively few number of iterations because a local time step is used instead of smaller global time step.

It is clear from figures (4)-(5) that chemical reaction actually begin after the oblique shock wave and in the shear layer near the lower and upper walls. As the inlet temperature is not high enough for combustion excitation (i.e. $T_{in} = 900\ [K] < 1000\ [K]$). Some fluctuation are observable in the Oxygen and Hydroxyl mass fractions, along the oblique shock wave. Since, the shock-initiated reactions of O_2 termination and OH formation are characterized by its very high rates as indicated by Rogers and Chinitz model. (19). In figure (6), it obvious that some week shocks formed at the leading edge of the duct in the lower and upper walls, followed by a stronger oblique shock wave, which reduce flow Mach number (M) about 50% of its value at the duct inlet. Besides, the boundary layer growth is observed, especially at the upper wall, where the boundary layer thickness reaches its maximum value at the duct exit. The maximum variation in the mixture specific heat ratio (γ_{mix}), is about 7.6% relative to its minimum value, which should be considered in the evaluation of frozen flow models. The pressure and temperature distributions are presented in figures (7) and (8), respectively. There is a rise in the static pressure following the oblique shock. It is considered as an evidence of the shock-induced combustion effect to increase the static pressure. However, the maximum temperature obtained at the viscous layers in the lower wall behind the shock, where static temperature is increased to 3300 $[K]$, due to the flow deceleration by the shock wave, and due to the shear effect at the adiabatic walls.

Figures (9)-(14) present the numerical solutions at the normal distance of 0.13 [cm] from the wall. The present numerical solutions of the three different meshes sizes(31×51, 61×51, and 91×51) are compared to the previous solutions of Chitsomboon et al. (30), and Shuen and Yoon (22). The present

solutions are unsensitive to grid resolution. Also, there is qualitative and quantitative agreement between the current results and the previous solution of Chitsomboon et al. (30). It is clear that the OH mass fraction solution is greatly dependent on the grid resolution. As, there are sharp fluctuations in its value, initiated at the shock regions. It can also be seen that by increasing the grid size in longitudinal direction, the fluctuations amplitude diminish but the frequency of fluctuations increases. This is due to the poor estimation of Rogers and Chinitz model (19) as discussed by Chitsomboon et al. (28). In addition, the present solutions give smooth rise in pressure across shock due to the diffusive effect of TVD scheme. There is a good agreement between the current estimation of the temperature and the published results (30).

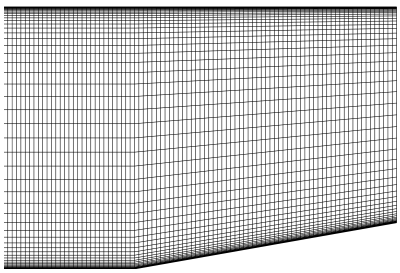

Figure 2 91×51 **mesh, used in solving turbulent flow in a ramped duct**

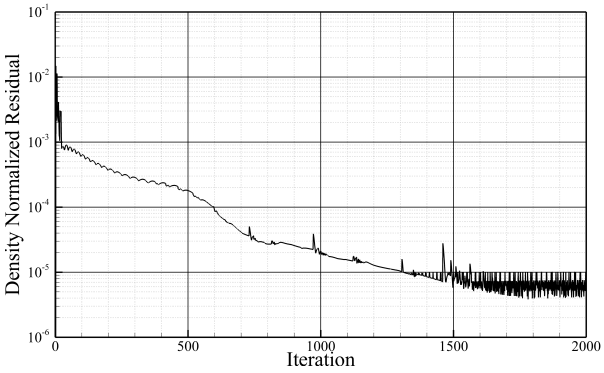

Figure 3 Convergence history of the case of turbulent premixed flow in a ramped duct for $T_{in} = 900\ [K]$**.**

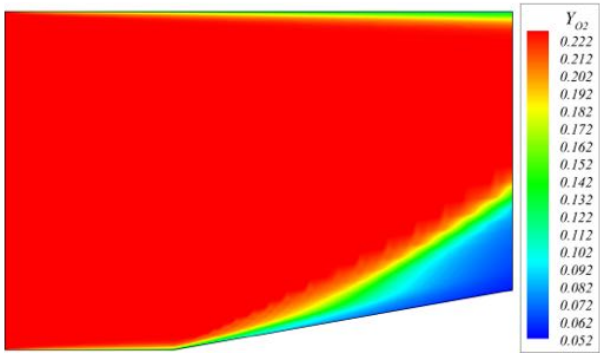

Figure 4 Mass fraction contours of Hydrogen (Y_{H_2}) **in case of turbulent reacting flow in a ramped duct for** $T_{in} = 900\ [K]$**.**

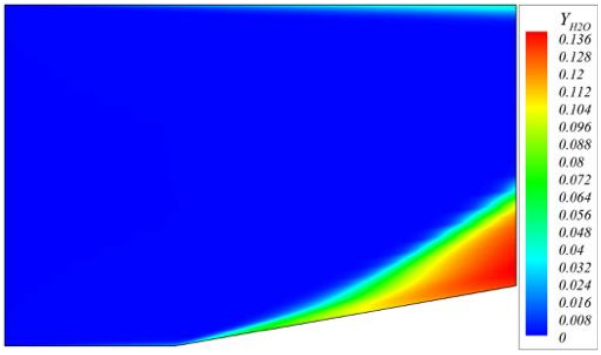

Figure 5 Mass fraction contours of water ($Y_{\mathrm{H}_2\mathrm{O}}$) **in case of turbulent reacting flow in a ramped duct for** $T_{in} = 900\ [K]$**.**

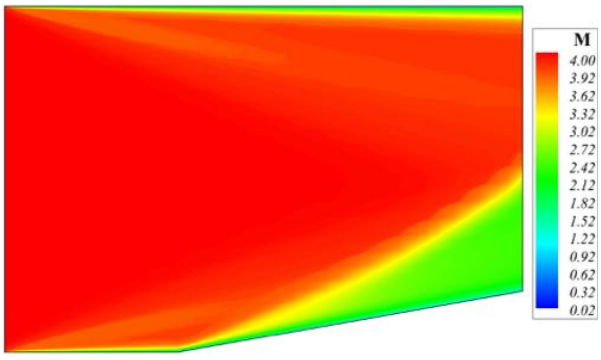

Figure 6 Mach Number (M) contours in case of turbulent reacting flow in a ramped duct for $T_{in} = 900\ [K]$**.**

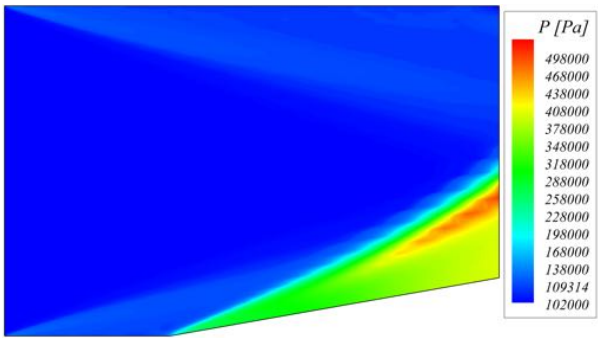

Figure 7 Pressure (P) contours in case of turbulent reacting flow in a ramped duct for $T_{in} = 900\ [K]$.

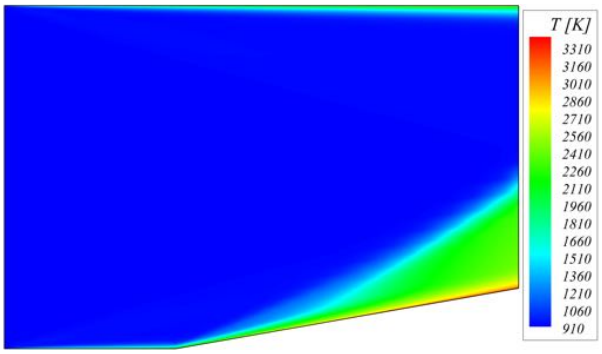

Figure 8 Temperature (T) contours in case of turbulent reacting flow in a ramped duct for $T_{in} = 900\ [K]$.

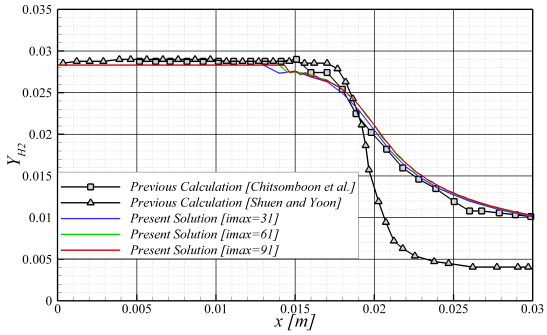

Figure 9 Present solution compared to previous calculations of ref. (30) and (22) for H_2 mass fraction at $0.13\ cm$ from the lower wall

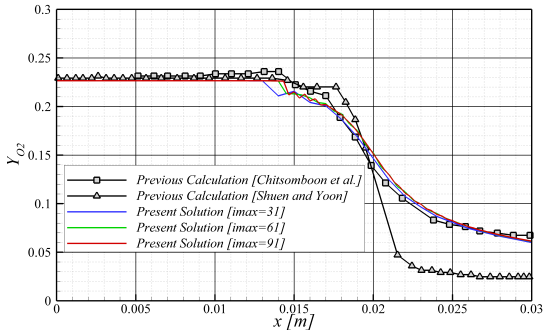

Figure 10 Present solution compared to previous calculations of ref. (30) and (22) for O_2 mass fraction at $0.13\ cm$ from the lower wall

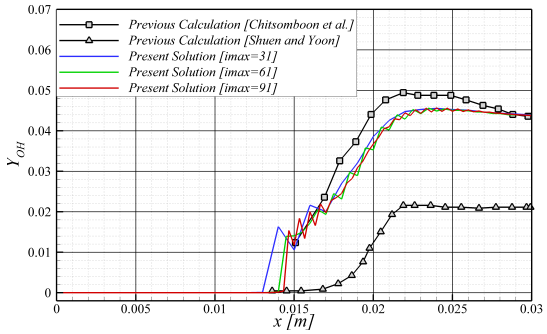

Figure 11 Present solution compared to previous calculations of ref. (30) and (22) for OH mass fraction at $0.13\ cm$ from the lower wall

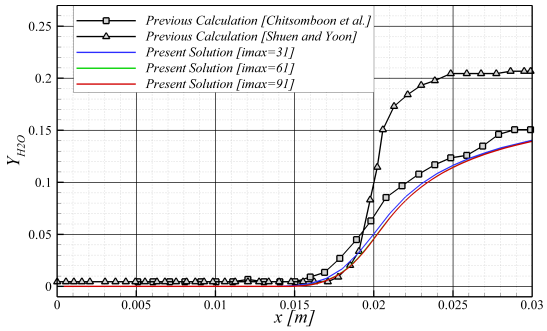

Figure 12 Present solution compared to previous calculations of ref. (30) and (22) for H_2O mass fraction at $0.13\ cm$ from the lower wall

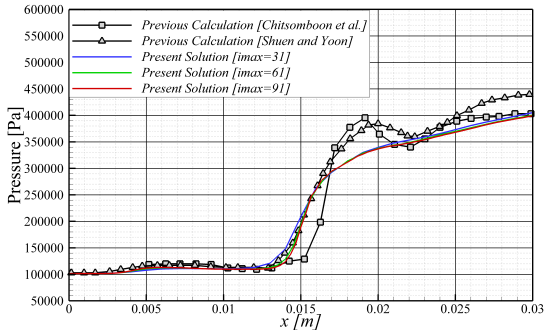

Figure 13 Present solution compared to previous calculations of ref. (30) and (22) for pressure at 0.13 cm **from the lower wall**

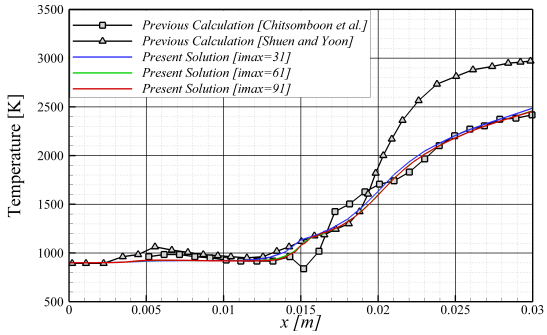

Figure 14 Present solution compared to previous calculations of ref. (30) and (22) for temperature at 0.13 cm **from the lower wall**

4.1.2 Reacting Inlet Flow Test Case

In the second case, when the inlet temperature exceeds the minimum limit of combustion initiation, (i.e. $T_{in} = 1200\ [K] > 1000\ [K]$), chemical reactions takes place starting from the duct inlet. However, the static temperature rise at the formed oblique shock wave accelerates significantly the chemical reaction rates.

Local time stepping is used for the pseudo time integration with CFL number equals to ($\sigma = 0.1$). A fast convergence is obtained after 1200 iterations as illustrated in figure (15). The density normalized residual is fluctuating below 10^{-5}.

As shown in figures (16)-(17), it is found that the reduction in Oxygen and Hydrogen mass fractions, and the increase in Hydroxyl and water mass fractions, start from the duct inlet. However, it is clear that O_2 and H_2 termination and OH and H_2O formation are accelerated after the oblique shock wave. The mass fractions of O_2 and H_2 is reduced after the shock by about 75% and 50% respectively, relative to their values at the inlet.

It is clear from figure (18) that the waves at the duct leading edges become weaker than that in the first case. The variation in flow Mach number (M) before the shock becomes smoother. That is due to the heat released from the exothermic chemical reactions initiated at the duct inlet. It is important to mention that the maximum static pressure attained in this problem does not exceed 4.0 [bar], which is lower than that achieved by the previous test case of lower inlet temperature. Even though the total inlet total pressure is higher in the second test case, the high static pressure is achieved in the first case. In the first case, the sudden reaction initiation across the shock wave in addition of the shock compression effect lead to sharp rise in static pressure only after the oblique shock wave. The thermal energy produced from the exothermic reactions is distributed in smaller region.

Figures (21)-(25) present the numerical solutions for three different meshe sizes, where the discretization in y-direction is constant (i.e. $jmax = 51$), and the mesh sizes in x-direction are $imax = 31,\ 61,$ and 91. The solutions are presented at a distance of 0.13 $[cm]$ from the lower wall. The results are compared with the previous results of Yee and Shinn (33) and that of Shuen and Yoon (22). The species concentrations are presented in figures (21)-(23), where there is a sudden decrease in Oxygen and Hydrogen mass fraction, and very steep rise in Hydroxyl concentration at the duct inlet. The results of O_2 and OH concentrations are greatly affected by the grid resolution at the duct inlet. However, there is a good agreement between the present solution and that of Yee and Shinn (33). In figure (25), the solution of Shuen and Yoon (22), has non-physical oscillations after the shock. The present results and the results of ref. (33) have no oscillation due to the diffusive effect of the TVD schemes. In figure (26), there is about 20 % variation between the present solution and that of ref. (22).

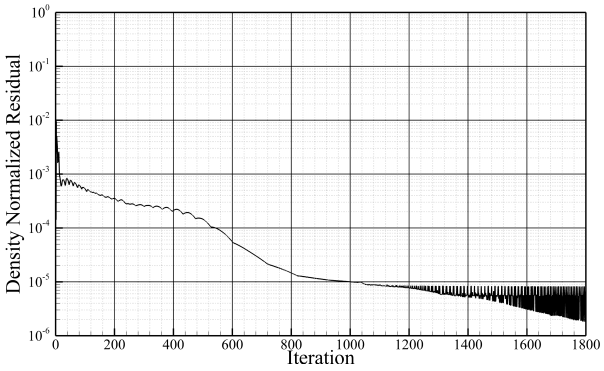

Figure 15 Convergence history of the case of turbulent premixed flow in a ramped duct for $T_{in} = 1200\ [K]$.

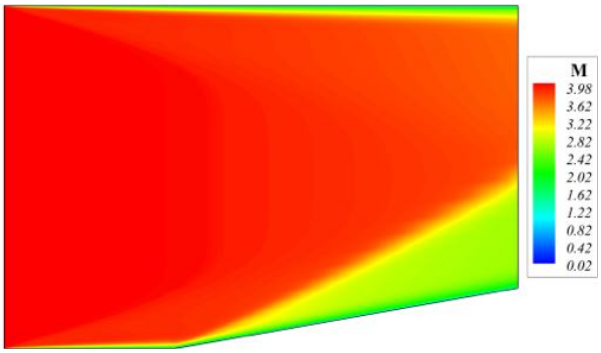

Figure 18 Mach number (M) contours in case of turbulent reacting flow in a ramped duct for $T_{in} = 1200\ [K]$.

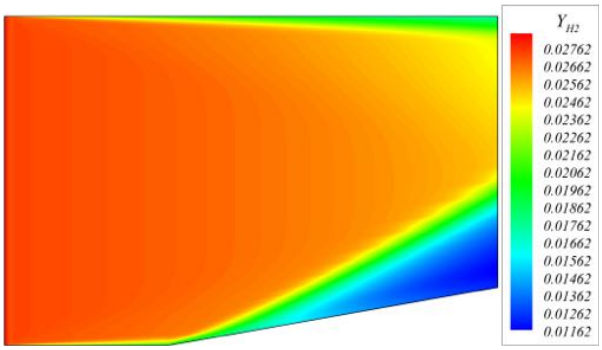

Figure 16 Mass fraction contours of Hydrogen (Y_{H_2}) in case of turbulent reacting flow in a ramped duct for $T_{in} = 1200\ [K]$.

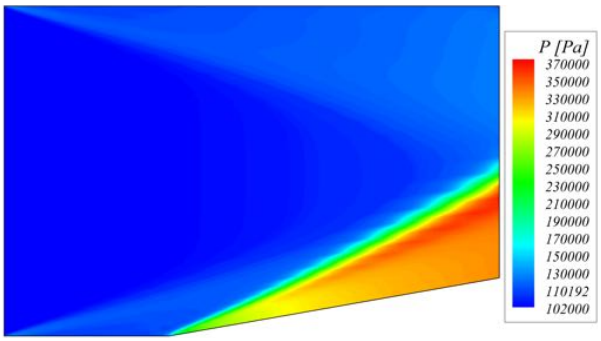

Figure 19 Pressure (P) contours in case of turbulent reacting flow in a ramped duct for $T_{in} = 1200\ [K]$.

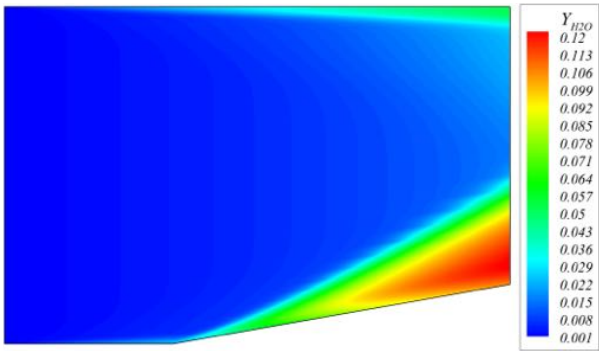

Figure 17 Mass fraction contours of water (Y_{H_2O}) in case of turbulent reacting flow in a ramped duct for $T_{in} = 1200\ [K]$.

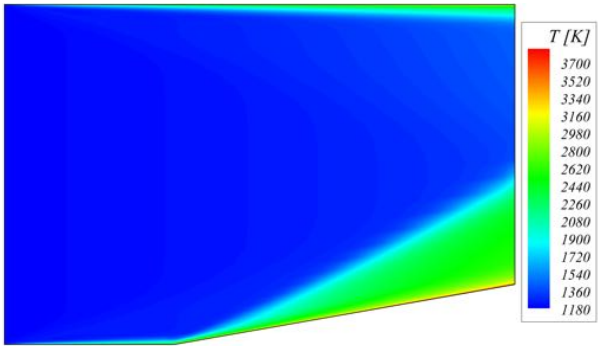

Figure 20 Temperature (T) contours in case of turbulent reacting flow in a ramped duct for $T_{in} = 1200\ [K]$.

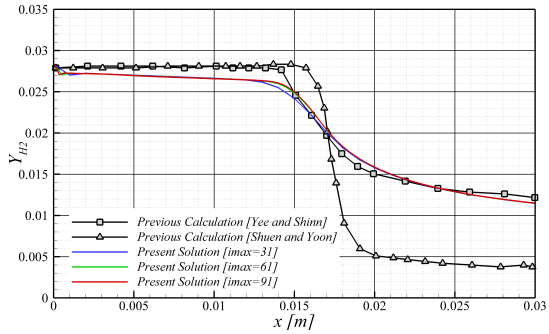

Figure 21 Present solution compared to previous calculations of ref. (33) and (22) for H_2 mass fraction at 0.13 cm from the lower wall

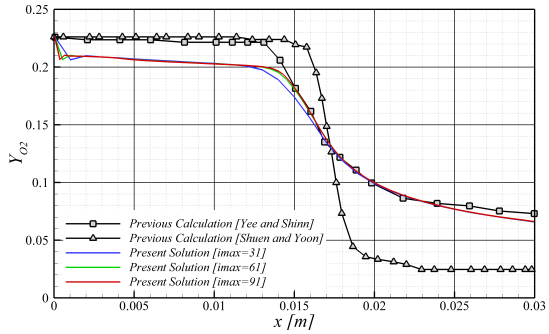

Figure 22 Present solution compared to previous calculations of ref. (33) and (22) for O_2 mass fraction at 0.13 cm from the lower wall

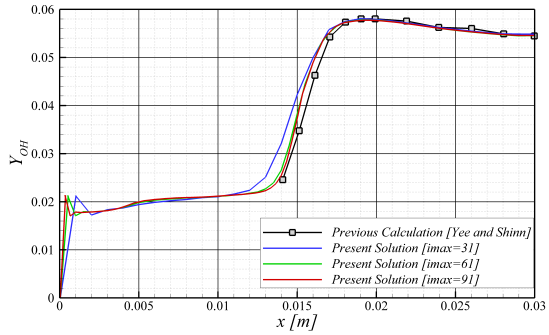

Figure 23 Present solution compared to previous calculations of ref. (33) for OH mass fraction at 0.13 cm from the lower wall

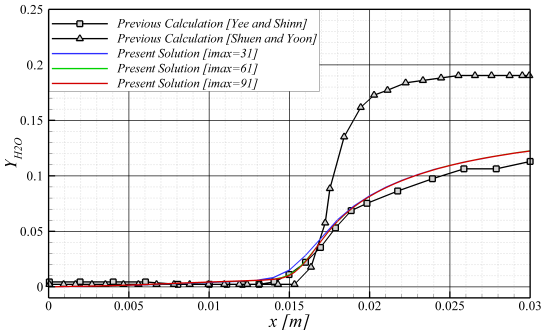

Figure 24 Present solution compared to previous calculations of ref. (33) and (22) for H_2O mass fraction at 0.13 cm from the lower wall

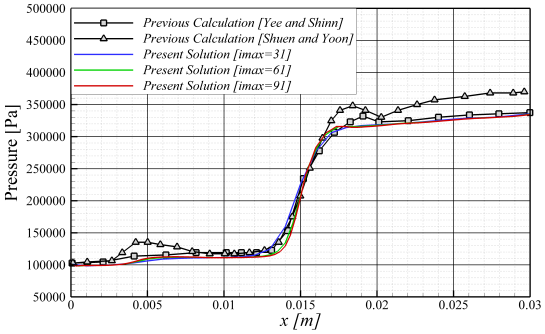

Figure 25 Present solution compared to previous calculations of ref. (33) and (22) for pressure at 0.13 cm from the lower wall

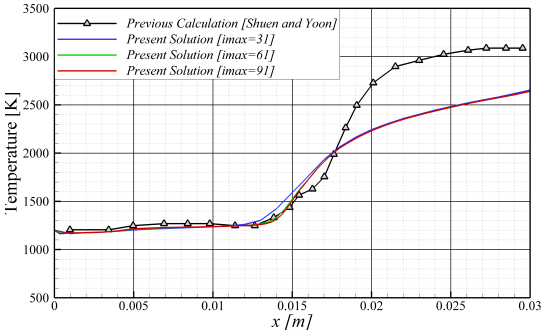

Figure 26 Present solution compared to previous calculations of ref. (22) for temperature at 0.13 cm from the lower wall

4.2 Mixing and Combustion Processes in Single-Strut Scramjet Engines

Non-reacting and reacting turbulent flow field in a 2D single strut scramjet engine model problem are

simulated in this study to investigate the effect of the transverse sonic fuel injection on the scramjet engine performance. The configuration of the problem is described in figure (27) as introduced by Drummond and Weidner (26). The engine length is 0.78 $[m]$, while its width at the inlet is 0.15 $[m]$. The middle fuel injection strut is 0.258 $[m]$ long and it is centered around the module minimum cross-section, which is located at 0.378 $[m]$ from the inlet leading edge. The half inclination angles of the injection-strut walls are 7.1 degrees. This geometry is a two-dimensional projection for an individual module of an actual scramjet engine design. Supersonic air flow enters from the intake, where gaseous Hydrogen is injected transversely at sonic speeds from four ports at the middle injection-strut located at 0.06 $[m]$ downstream from the minimum cross-section. The injection opening taken to be 0.1 $[cm]$ such that the overall equivalence ratio of air- hydrogen mixture is one. The inlet conditions of both air and Hydrogen are given as follows,

$$\begin{array}{ll} \mathbf{M}_{in_{air}} = 5.03 & T_{in_{air}} = 335.0\ [K] \\ P_{in_{air}} = 3546.0\ [Pa] & T_{in_{\mathrm{H}_2}} = 246.0\ [K] \\ P_{in_{\mathrm{H}_2}} = 254824.0\ [Pa] & \end{array} \tag{71}$$

The longitudinal module length is assumed to be the reference length (L_{ref}), while the air inlet properties is used for the other reference variables as given below,

$$\begin{array}{ll} L_{ref} = 0.78\ [m] & \rho_{ref} = \rho_{in_{air}} \\ T_{ref} = T_{in_{air}} & V_{ref} = V_{in_{air}} \\ \mu_{ref} = \mu_{L_{in_{air}}} & k_{ref} = k_{L_{in_{air}}} \\ \mathcal{D}_{ref} = \mathcal{D}_{L_{in_{air}}} & \end{array} \tag{72}$$

Only the upper half of the scramjet model is considered in the simulation and symmetrical boundary conditions are applied at the engine centerline. Meshes of sizes 87×31 and 200×51, are employed for domain discretization. The second mesh is shown in figure (28). The grid lines are clustered near the wall surface and around the vertical line ($x = x_o = 0.378\ [m]$) at which Helium is injected from the lower wall. The governing equations are integrated in time using the global and minimum value of time step with CFL number of 0.1. Time stepping is not applied in this case as suggested by Chitsomboon et Tiwari (28).

4.2.1 Non-reacting Turbulent Flow Case

By isolating the effect of the chemical reaction on the flowfield inside the scramjet engine module, the simulation demonstrates the role of shock system and recirculation zones created around the transverse injection in the mixing process and flame holding. The distribution of Hydrogen mass fraction in that case is used as an to monitor the mixing enhancement using transverse injection. In addition, the static temperature distribution in the non-reacting case is examined to find the combustion-stabilization zones upstream the injectors. Two opposite injectors are placed near the minimum cross-section of the engine in order to guarantee effective mixing process. Also, the mixing is enhanced by raising the injection pressure relative to the air flow to force the fuel penetration into the supersonic main flow. The injection pressure is about 70 times the air flow static pressure.

As shown in figures (29)-(30) for a mesh size of 200×51. Recirculation zone is created in the engine intake due to shock-wave/boundary-layer interactions. Mach number contours show clearly an oblique shock wave originated from the intake leading edge then reflected at the middle strut apex to the upper wall. Shock wave reflection creates a relatively high speed recirculation zone. Then the flow goes through complicated system of shock reflection and separation shock at the module minimum cross-section. The shock waves deflects airflow direction parallel to the injection strut walls leading to large vortical zone adjacent to the engine wall. The upstream vortical flow speed is higher than that of the other downstream recirculation zones which leads to static temperature increase up to $2300[K]$ in the turbulent shear layers as shown in figure (32). The recirculation zone, upstream of the injector at the middle strut wall, extends upstream to pass through the minimum cross-section. H_2-air mixing is carried out in the vortical flow front of the injection region, as illustrated in figure (31). After the injection region, the mixture is then expanded, where Hydrogen diffusively transfers into air as mixing layers.

The solutions of the two mesh sizes (87×31 and 200×51) are compared to each other. Comparisons are carried out in terms of normalized variables to facilitate the evaluation of the different sets of results. The utilized normalized variables are the axial and transversal normalized distance; x_{norm}, and y_{norm} respectively, in addition to the normalized pressure (P_{norm}). They are expressed as follows,

$$\begin{aligned} x_{norm} &= \frac{x - x_{\text{intake leading edge}}}{x_{\text{intake leading edge}} - x_{\text{nozzle trailing edge}}} \\ y_{norm} &= \frac{y - y_{min}}{y_{max} - y_{min}} \end{aligned} \tag{73}$$

The results of the non-reacting case at different stations upstream and downstream the injection ports for mesh sizes of 87×31 and 200×51 are compared with the previous calculations. Solutions of H_2 mass fraction, and static temperature, at different axial normalized distances are presented in figure (33) and (34). Stations of axial normalized distance ranging between 0.51 and 0.55 represent the flow domain upstream the injection ports, while those ranging between 0.57 and 0.61 represent the downstream flowfield.

The solutions of 87×31-sized mesh underestimate the H_2 mass fraction upstream the injection port. Refining the mesh to a size of size 200×51 enables to predict accurately the flowfield as shown in the results of the Hydrogen mass fraction. The 200×51 results show that H_2-air mixing is more effective at the module wall than that at the middle strut surface because larger size of the recirculation zone formed adjacent to the upper wall as presented in figure (30).

Based on the simulation results for the non-reacting case, it is clear that there are recirculation zones of low speed and high temperature are created upstream the injection ports. And that helps in the flame self-ignition and stabilization for supersonic combustion. Also, the fuel-air mixing is improved, as the shocks created upstream the injector decelerate the incoming supersonic air flow, in order to be turbulently mixed with injected hydrogen in the transverse direction.

4.2.2 Reacting Turbulent Flow Case

The unsteady Navier-Stocks equations are solved using a minimum time step with CFL number of 0.1. A system of equations composed of eight coupled non-linear partial differential equations are solved. Four reacting species (i.e. O_2, H_2, OH, and H_2O) are considered in the simulation while Nitrogen is assumed to be inert.

A mesh size of 200×51 is used in the simulation of the reacting and turbulent H_2-air flow inside scramjet engine, which is the greater than the mesh size employed in Drummond and Weidner (26), and Chitsomboon et al. (29). The results of this simulation are presented in figures (35)-(39). It is clear from the results that the recirculation zones upstream the minimum cross-section becomes larger compared to the non-reacting case due to the increase in the static temperature inside the injection zone. The static temperature is raised to 3300 $[K]$ approximately in the flow-separation region upstream the injectors. Static temperature increases close to the impact zone of the vortex flow with perpendicular H_2 injection.

Hydrogen mass fraction is nearly zero in the front of the recirculation zones and it is also reduced in the free mixing layer along the engine module as shown in figure (38) which indicates to an enhancement of the mixing and flame-holding processes due to the formation of these vortical structures. The magnitude of water mass fraction demonstrates the extent of the combustion along the flow field. Combustion is mainly initiated and sustained by means of the separating shocks in front of the injected H_2 stream as shown in figure (37). It is clear from figure (39), that the flame-holding recirculation zones have simpler eddy-structure compared to the non-reacting test case because the separation intensity is diminished as a result of the total temperature increase in the combustion zone.

In figures (43) and (41) present the solutions of temperature and water mass fraction at different stream-wise stations in the engine. They are *qualitativaly* compared with the previous solutions of Chitsomboon et al (29) shown in figure (42) and (44). Point-to-point comparison is unavailable, because the x-stations coordinates are not given in ref. (29).

As illustrated in figures (42) and (41), the H_2O mass fraction solution of the 87×31-sized mesh of Chitsomboon et al. (29), is less than predicted by the present solution utilizing 200×51-sized mesh. It is noted that the magnitude of H_2O does not significantly change as an indication of fuel-air mixing efficiency in the recirculation zones. In addition, qualitative analysis between the normalized temperature of previous solution and the static temperature of the present solution shows resemblance in temperature field downstream the injectors While the present solution predicts almost constant static temperature in the front recirculation zones.

The results of the normalized pressure on the engine upper wall surface are compared with the calculations of Chitsomboon et al. (29). In figure (45), the normalized pressure is presented along the whole engine module, where the normalized pressure for all solutions equal to unity at the injection zone. The previous solution of the reacting case agrees with the non-reacting solution of the same mesh

size (87×31). The normalized pressure is given as follow,

$$P_{norm} = \frac{P - P_{\text{air inlet}}}{P_{\text{H}_2 \text{ injection}} - P_{\text{air inlet}}} \tag{74}$$

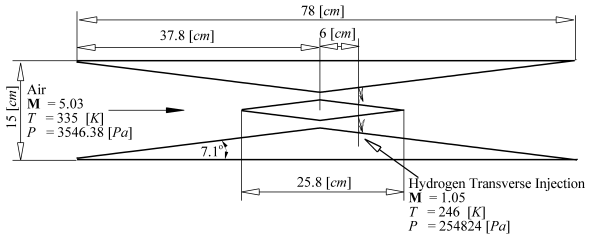

Figure 27 Schematic diagram for single two-dimensional strut Scramjet Engine

Figure 28 200×51 **mesh, used in solving turbulent 2D flow in single strut scramjet engine**

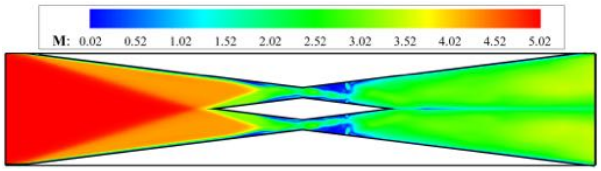

Figure 29 Mach number (M) contours of the non-reacting case solution, for mesh size 200×51

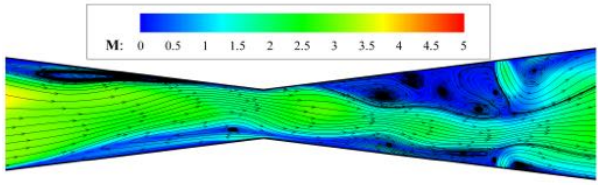

Figure 30 Mach number (M) contours within the upper injection zone, for the non-reacting case solution, for mesh size 200×51

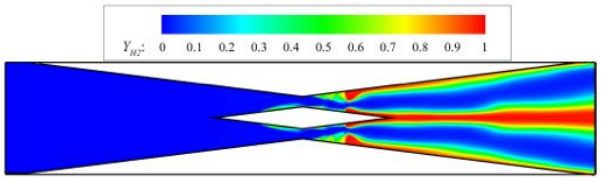

Figure 31 Hydrogen mass fraction (Y_{H_2}) contours of the non-reacting case solution, for mesh size 200×51

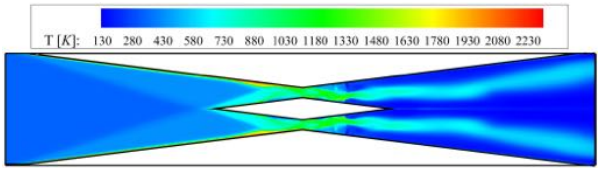

Figure 32 Temperature (T) contours of the non-reacting case solution, for mesh size 200×51

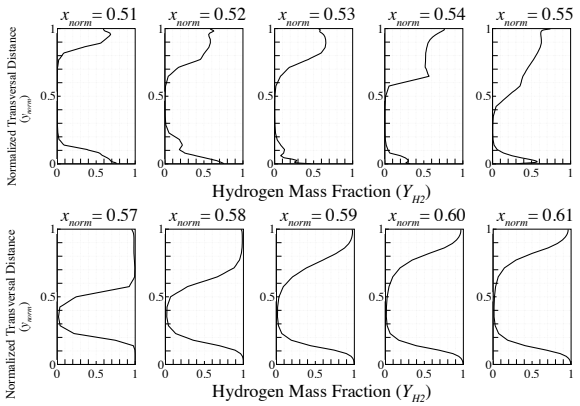

Figure 33 Hydrogen mass fraction solution at different station, for the non-reacting case for mesh size 200×51

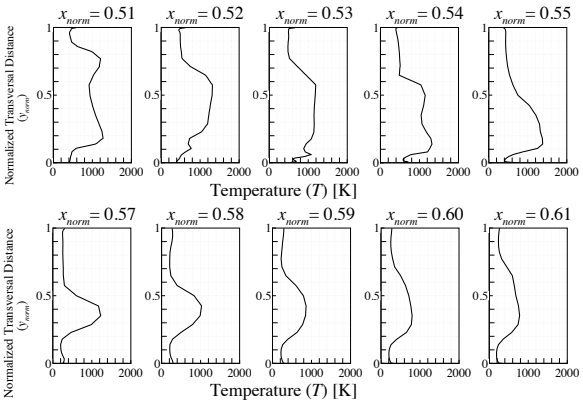

Figure 34 Temperature solution at different station, for the non-reacting case for mesh size 200×51

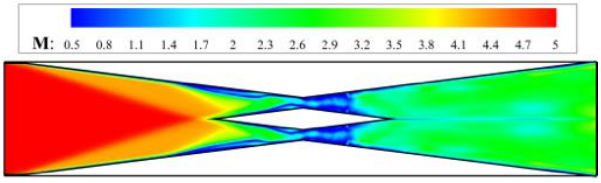

Figure 35 Mach number (M) contours of the reacting case solution, for mesh size 200×51

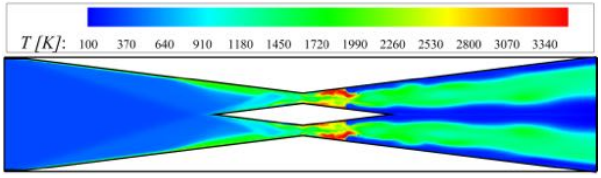

Figure 36 Temperature (T) contours of the reacting case solution, for mesh size 200×51

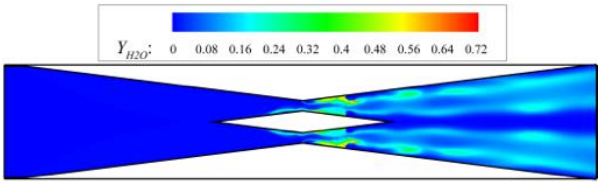

Figure 37 Water mass fraction ($Y_{\mathrm{H_2O}}$) contours of the reacting case solution, for mesh size 200×51

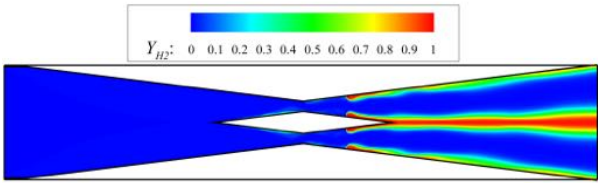

Figure 38 Hydrogen mass fraction ($Y_{\mathrm{H_2}}$) contours of the reacting case solution, for mesh size 200×51

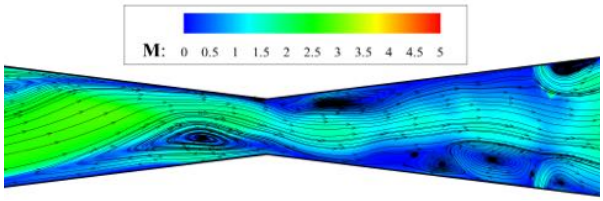

Figure 39 Mach number (M) contours within the upper injection zone, for the reacting case solution, for mesh size 200×51

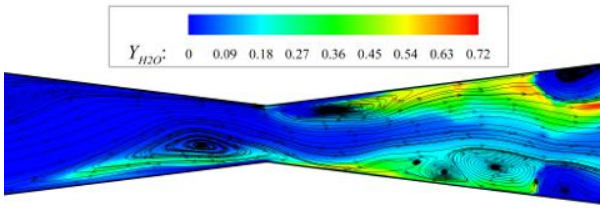

Figure 40 Water mass fraction ($Y_{\mathrm{H_2O}}$) contours within the upper injection zone, for the reacting case solution, for mesh size 200×51

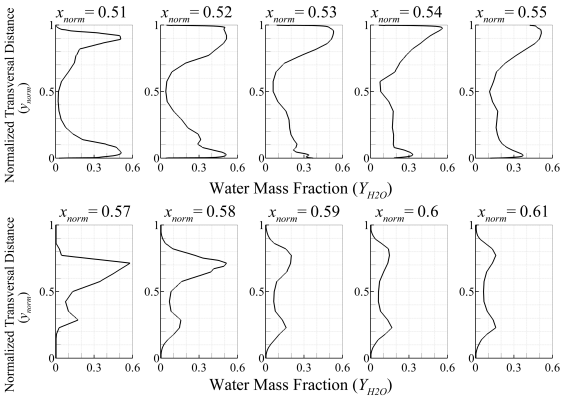

Figure 41 Water mass fraction solution at different station, for the reacting case for mesh size 200×51

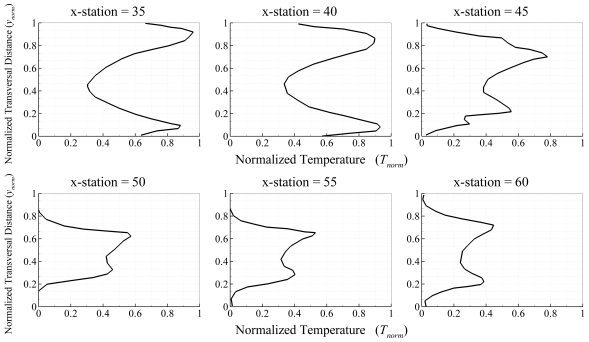

Figure 44 Previous solution for normalized temperature at different station, for the reacting case (ref. (29))

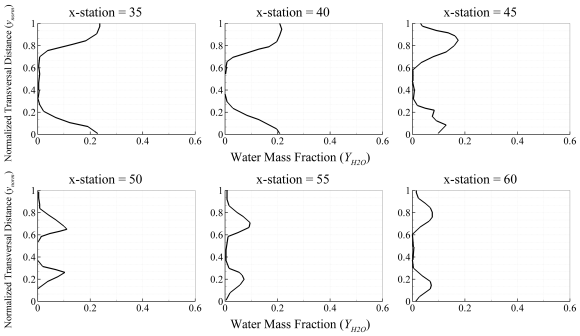

Figure 42 Previous solution for water mass fraction at different station, for the reacting case (ref. (29))

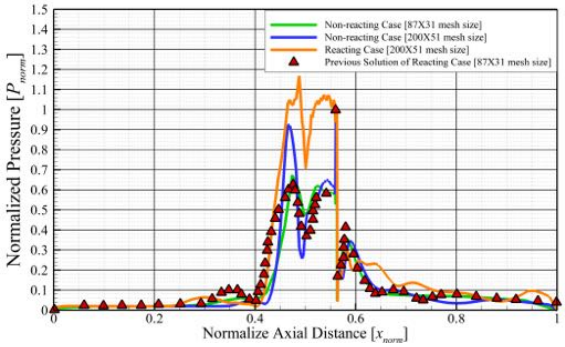

Figure 45 Normalized pressure solution on the upper wall, compared to the previous solution (ref.(29))

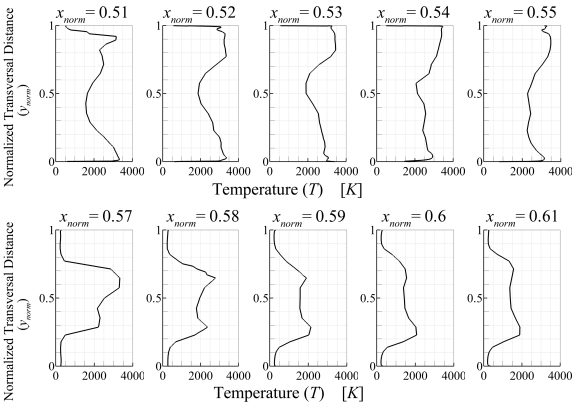

Figure 43 Temperature solution at different station, for the reacting case for mesh size 200×51

5 Conclusion

Development of scramjet engines of satisfactory performance requires enhancement of the fuel-air mixing and flame stabilization. The effect of transverse sonic fuel injection on fuel-air mixing and flame stabilization is investigated numerically in the current study. A numerical tool is developed using the Reynolds Average Navier-Stokes equations. Chemical kinetics model is employed to compute the finite rates of the chemical reactions. Zero-equation of Baldwin-Lomax are used to calculate the turbulent eddy viscosity. Finite-volume scheme is applied where the convective fluxes are discretized by second order accurate Roe's scheme using MUSCL approach. Second order accurate Runge-Kutta method is used for the time-integration. The convective and viscous flow fluxes are treated explicitly, where only

the chemical source term is solved implicitly in order to reduce the computational efforts of inverting the flow Jacobians. The problem of Helium transverse sonic injection into supersonic air flow is simulated and the results are compared with the previous investigations. In addition, air-hydrogen flow is studied in a single strut scramjet engine, where mixing and flame holding processes are carried out using fuel transverse sonic injection. The simulation shows that high adverse pressure gradient is created near the injection zone. Thus, a separation shock is formed with a recirculation zone in front of the injection region and the combustion process is sustained. The results are compared with previous numerical and experimental investigations and the results are in good agreement with the published data.

References

[1] J. P. Drummond, J. P. (1979). **"Numerical Investigation of the Perpendicular Injector Flow Field in a Hydrogen Fueled Scramjet"**, J. P. Drummond, NASA Langley Research Center, Hampton, Va. AIAA 12^{th} FLUID AND PLASMA DYNAMICS CONFERENCE July 23-25, 1979 / Williamsburg,Virginia

[2] Farshchi, M., **"Supersonic Turbulent Reacting Flow Modeling and Calculation"**, Technical Report NASA-CR-196185, National Aeronautics & Space Administration, Lewis Research Center, April 1991.

[3] Drummon d, J. P.; Rogers, R. C.; and Evans, J. S. , **"Combustor Modeling for Scramjet Engines"**, AGARD CP 275. Presented at AGARD Combustor Modeling, Cologne, Oct. 1979.

[4] Cinnella, P. and Grossman, B., **"Computational Methods for Chemically Reacting Flows"**, Handbook of Fluid Dynamics and Fluid Machinery, Wiley and Sons, New York, 1996, pp. 1541"1590.

[5] Spalart, P. R.; Jou, W. H.; Strelets, M.; and Allmaras, S. R., **"Comments on the Feasibility of LES for Wings, and on a Hybrid RANS/LES Approach"**, In 1^{st} AFOSR International Conference on DNS/LES, Aug. 1997.

[6] Tannehill, J.C.; Anderson, D.A.; and Pletcher, R.H., **"Computational Fluid Mechanics And Heat Transfer"**, Second Edition, published by Taylor & Francis Ltd., London, UK, 1997.

[7] Chou, P. Y., **"On the Velocity Correlations and the Solution of the Equations of Turbulent Fluctuation"**, Quart. Appl. Math., Vol. 3, p.38.

[8] Davidov, B.I., **"On the Statistical Dynamics of an Incompressible Fluid"**, Doklady AN. SSSR, Vol. 136, p. 47.

[9] Kolmogorov, A. N., **"Equations of turbulent Motion of an Incompressible Fluid"**, Isvestia Academy of Sciences, USSR; Physics, Vol. 6, No. 1 and 2, pp. 56−58.

[10] Baldwin, B.S. and Barth, T.J., **"A One-Equation Turbulence Transport Model for High Reynolds Number Wall-Bounded Flows"**, NASA Technical Memorandum-102847, 1991.

[11] Smith, A.M.0. and Cebeci, T., **"Numerical Solution of the Turbulent Boundary-Layer Equations"**, Douglas Aircraft Division Report DAC 3373.

[12] Baldwin , B.S. and Lomax, H., **"Thin Layer Approximation and Algebraic Model for Separated Turbulent Flows"**, AIAA Paper 78−257, 16^{th} Aerospace Sciences Meeting, January 1978.

[13] Degani, D. and Schiff, L.B., **"Computation of Supersonic Viscous Flows Around Pointed Bodies at Large Incidence**" AIAA Paper 83−0034, AlAA 21^{st} Aerospace Sciences Meeting, January 1983.

[14] Mottura, L.; Vigevano, L., and Zaccanti, M. (2000). **"Factorized Implicit Upwind Methods Applied to Inviscid Flows at High Mach Number"**, AIAA Journal, Vol. 38, No. 10, October 2000.

[15] Yoon, S., and Jameson, A., **"Lower-Upper Symmetric Gauss-Seidel Method for Euler and Navier-Stocks Equations"**, AIAA Journal, Vol. 26, No. 9, pp. 1025−1026, September 1988.

[16] Curtiss, C.F. and Hirschfelder, J.O., **"Integration of Stiff Equations"**, Proc. National Academy of Sciences of the USA, Vol. 38, 1952.

[17] Grossman, B. and Cinnella, P., **"Flux-Split Algorithms For Flows With Non−Equilibrium Chemistry And Vibrational Relaxation"**, Journal of Computational Physics 88, pp. 131−168, 1990.

[18] Walters, R.W.; Cinnella, P.; Slack, D.C.; and Halt, D., **"Characteristic−Based Algorithms for Flows in Thermo−Chemical Nonequilibrium"**, AIAA Paper 90−0393, 28th Aerospace Sciences Meeting, January 1990.

[19] Rogers, R.C. and Chinitz, W., **"Using a Global Hydrogen−Air Combustion Model in Turbulent Reacting Flow Calculations"**, AIAA Journal Vol. 21, No. 4, pp. 586−592, April 1983.

[20] (a) Bussing, T.R.A. and Murman, E.M., **"A Finite Volume Method For The Calculation of Compressible Chemically Reacting Flows"**, AlAA Paper 85−0331, 23rd Aerospace Sciences Meeting, January 1985.

[21] (b) Bussing, T.R.A. and Murman, E.M., **"Numerical Investigation of 2−Dimensional H_2 −Air Flame Holding Over Ramps And Rearward Facing Steps"**, AIAA Paper 85−1250, 21st Joint Propulsion Conference, July 1985.

[22] Shuen, J.S. and Yoon, S., **"Numerical Study of Chemically Reacting Flows Using an LU Scheme"**, AIAA Journal, Vol. 27, No. 12, pp. 1752−1760, December 1989.

[23] Hitch, B.D.; Laxter, W.R.; Senser, D.W.; and Sojka, P.E., **"On the Selection of H_2/Air Kinetic Mechanisms for Use in Supersonic Combustor Modeling"**, presented at the Spring 1986 Technical Meeting of the Central States Section of the Combustion Institute, May 1986.

[24] Eklund, D. R.; Hassan, H. A.; and Drummond, J. P., **"Time Efficient Calculation of Chemically Reacting Flow"**, AIAA Paper No. 86-0563, January 1986.

[25] Drummond, J.P.; Hussaini, M.Y. and Zang, T.A., **"Spectral Methods for Modeling Supersonic Chemically Reacting Flow Fields"**, AlAA Paper 85−0302, 23rd Aerospace Sciences Meeting, January 1985.

[26] Drummond, J.P. and Weidner, E.H. , **"NumericalS tudy of a Scramjet Engine Flow Field"**, AlAA 19th Aerospace Sciences Meeting, January 1981.

[27] Chitsomboon, T. and Tiwari, S. N., **"Investigation of Chemically Reacting Supersonic Internal Flows"**, Department of Mechanical Engineering and Mechanics, School of Engineering, Old Dominion University. Technical Report, NAG-1-423, September 1985.

[28] Chitsomboon, T. and Tiwari, S.N., **"Numerical Study of Hydrogen−Air Supersonic Flow By Using Ellipitic And Parabolized Equations"**, Progress Report for the period December 1 1985 to May 31 1986, Prepared for NASA, Langley Research Center, Hampton, Virginia, USA, August 1986.

[29] Chitsomoon, T.; Kumar, A.; Drummond, J.P. and Tiwari, S.N., **"Numerical Study of Supersonic Combustion Using A Finite−Rate Chemistfw Model"**, AlAA Paper 86−0309, 24th Aerospace Sciences Meeting, January 1986.

[30] Chitsomboon, T.; Kumar, A. and Tiwari, S.N., **"Numerical Study of Finite−Rate Supersonic Combustion Using Parabolized Equations"**, AIAA Paper 87−0088, 25th Aerospace Sciences Meeting, January 1987.

[31] McBride, B.J.; Gordon, S. and Reno, M.R., **"Coefficients for Calculating Thermodynamic and Transport Properties of Individual Species"**, NASA Technical Memorandum 4513, October 1993.

[32] Roe, P.L., **"Approximate Riemann Solvers, Parameter Vectors, and Difference Schemes"**, Journal of Computational Physics, Vol. 43, No. 2, pp. 357−372, October 1981.

[33] Yee, H.C. and Shinn, J.L., **"Semi-Implicit and Fully Implicit Shock-Capturing Methods for Hyperbolic Conservation Laws with Stiff Source Terms"**, 8 th Computational Fluid Dynamics Conference, AIAA, New York, 1987, pp. 159-176. (NASA Technical Memorandum–89415).

[34] Anderson, J.D., **"Hypersonic and High Temperature Gas Dynamics"**, American Institute of Aeronautics and Astronautics Inc., Reston, Virginia, USA, 2006.